# Chiral-Selective $CoSO_4/SiO_2$ Catalyst for (9,8) Single-Walled Carbon Nanotube Growth

**Hong Wang,[†] Li Wei,[†] Fang Ren,[‡] Qiang Wang,[†] Lisa D. Pfefferle,[‡] Gary L. Haller,[‡] and Yuan Chen[†,*]**

[†]School of Chemical and Biomedical Engineering, Nanyang Technological University, 62 Nanyang Drive, Singapore 637459 and [‡]Department of Chemical & Environmental Engineering, Yale University, New Haven, Connecticut 06520, United States

**ABSTRACT**

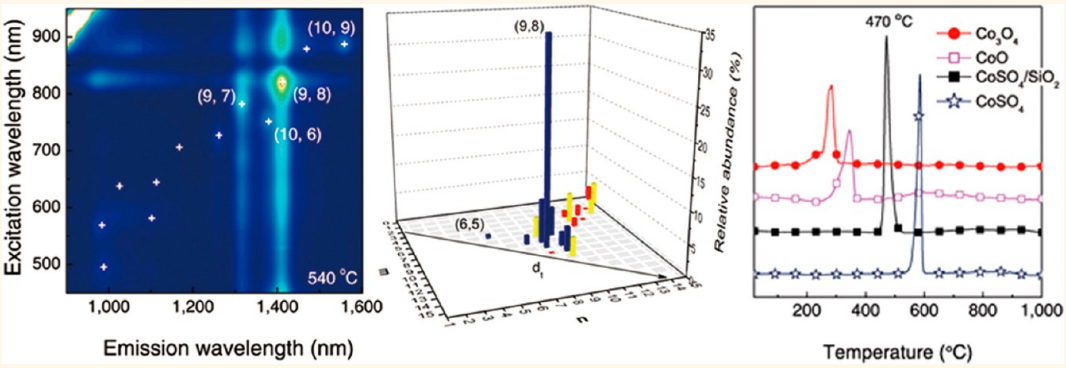


Electronic and optical properties of single-walled carbon nanotubes (SWCNTs) correlate with their chiral structures. Many applications need chirally pure SWCNTs that current synthesis methods cannot produce. Here, we show a sulfate-promoted $CoSO_4/SiO_2$ catalyst, which selectively grows large-diameter (9,8) nanotubes at 1.17 nm with 51.7% abundance among semiconducting tubes and 33.5% over all tube species. After reduction in $H_2$ at 540 °C, the catalyst containing 1 wt % Co has a carbon yield of 3.8 wt %, in which more than 90% is SWCNT. As compared to other Co catalysts used for SWCNT growth, the $CoSO_4/SiO_2$ catalyst is unique with a narrow Co reduction window under $H_2$ centered at 470 °C, which can be attributed to the reduction of highly dispersed $CoSO_4$. X-ray absorption spectroscopy (XAS) results suggested the formation of Co particles with an average size of 1.23 nm, which matches the diameter of (9,8) tubes. Density functional theory study indicated that the diameter of structurally stable pure Co particles is scattered, matching the most abundant chiral tubes, such as (6,5) and (9,8). Moreover, the formation of such large Co particles on the $CoSO_4/SiO_2$ catalyst depends on sulfur in the catalyst. XAS results showed that sulfur content in the catalyst changes after catalyst reduction at different conditions, which correlates with the change in (*n*,*m*) selectivity observed. We proposed that the potential roles of sulfur could be limiting the aggregation of Co atoms and/or forming Co—S compounds, which enables the chiral selectivity toward (9,8) tubes. This work demonstrates that catalysts promoted with sulfur compounds have potentials to be further developed for chiral-selective growth of SWCNTs.

**KEYWORDS:** carbon nanotubes · chirality · supported catalysts · cobalt · sulfur

Applications in electronics and medicine need chirally pure single-walled carbon nanotubes (SWCNTs).[1] A major obstacle for SWCNT applications is that the current synthesis methods produce SWCNTs with different (*n*,*m*) structures, leading to mixtures with distinct electronic properties ranging from metal to semiconductors with different band gaps.[2] Although single chirality nanotubes can be separated from SWCNT mixtures through different techniques,[3−6] the yield, scalability, and cost of such separation, as well as the property (length and functionality) of resulting SWCNTs, depend on the initial chirality distribution in SWCNT mixtures, which are determined during growth. SWCNTs are commonly grown by organizing atomic carbon species into thermodynamically stable cylinders on catalytic particles.[7] Depending on the nanotube diameter and the rolling angle of graphene sheet (chiral angle), the chiral structure of a SWCNT is indexed as two integers (*n*,*m*). Catalytic particles play critical roles in catalyzing the conversion of

* Address correspondence to chenyuan@ntu.edu.sg.

Received for review October 15, 2012 and accepted December 5, 2012.

**Published online December 05, 2012**
10.1021/nn3047633

© 2012 American Chemical Society

carbon-containing feedstocks, annealing defects of growing nanotubes, preventing SWCNT tip closure, terminating edge dangling bonds, and providing critical carbon density.[8−19] It has been suggested that chirality selectivity is related to the nucleation of carbon species on catalytic particles[15,16,20,21] and the different growth rates depending on the chiral angle of tubes.[13,14,22−24] Thus, catalytic particle composition and growth conditions may change the chiral selectivity. Several catalysts have shown chiral-specific growth, including Co/Mo,[25] Fe/Co,[26] Fe/Ru,[27] Fe/Ni,[28] Fe/Cu,[29] Co/Pt,[30] Co/Si,[31] Co/Ni-MCM-41,[32,33] and Co-TUD-1.[34] Their selectivity can be tuned to some extent by temperature,[35,36] catalyst support,[36,37] carbon feedstock,[36,38] pressure,[39] and crystal plane.[40] However, most current chiral-specific growth is restricted to one or two small-diameter chiral SWCNTs, such as (6,5) and (7,5). For example, the Co−Mo catalyst yields 62% of (6,5) and (7,5) tubes together (and 55% of (6,5)) among all semiconducting species.[25] Besides, the total carbon (SWCNT) yield of many reported chiral-specific growth is very low, resulting in the difficulty in achieving scalable production of desired SWCNTs. Recent experimental reports suggest that when $O_2$,[41] $CO_2$,[42] or $NH_3$[43] is introduced in synthetic conditions, some large-diameter SWCNTs can be synthesized with either metallicity selectivity or narrow chiral distribution.[42] Nevertheless, considering that there are more than 100 different chiral SWCNTs with diameters just between 0.6 and 1.5 nm, novel catalysts with specific single chirality selectivity are highly pursued.

In this work, we show that a novel sulfate-promoted catalyst has excellent selectivity toward large-diameter (9,8) nanotubes. SWCNTs were characterized by comprehensive characterization techniques, including Raman, photoluminescence (PL), UV−vis−near-infrared (UV−vis−NIR) spectroscopy, thermogravimetric analysis (TGA), transmission electron microscopy (TEM) and atomic force microscopy (AFM). The catalysts were analyzed by scanning electron microscopy (SEM), TEM, X-ray diffraction (XRD), nitrogen physisorption, UV−vis spectroscopy, $H_2$ temperature-programmed reduction ($H_2$-TPR), X-ray absorption spectroscopy (XAS) at the Co *K*-edge and the sulfur *K*-edge. Theoretical simulation of $Co_n$ particles was carried out. Possible mechanisms were proposed to explain the chiral selectivity toward (9,8) tubes and the plausible contribution of sulfur to the chiral selectivity.

## RESULTS AND DISCUSSION

The $CoSO_4/SiO_2$ catalyst was prepared by impregnating $CoSO_4$ on high surface area (254 $m^2/g$) fumed $SiO_2$ with ~1 wt % Co. The catalyst was used to catalyze SWCNT growth in a continuous-flow tubular chemical vapor deposition reactor. It was reduced in $H_2$ at 540 °C before exposed to 6 bar CO at 780 °C. In another experiment, the catalyst was reduced at 780 °C for 30 min and then exposed to CO. The collected solid carbon products were first characterized by Raman spectroscopy at three excitation wavelengths (785, 633, and 514 nm) shown in Figure 1a,b. The presence of the radial breathing mode (RBM) peaks between 100 and 350 $cm^{-1}$ and the low ratio of the D-to-G band intensities indicated that samples consist primarily of SWCNTs. The sample produced after reduction at 540 °C consists of fewer RBM peaks centered around 202−215 $cm^{-1}$ compared with the sample produced after 780 °C reduction. The chiral indexes (*n*,*m*) of RBM peaks are assigned based on empirical and theoretical Kataura plots (see Figures S1−S4, Table S1, and detailed discussion in the Supporting Information). The most intense RBM peaks belong to (12,3), (9,9), (15,0), (14,2), (13,4), (12,5), (13,3), (9,8), and (9, 7) tubes, which are highlighted as red bars ((9,8) and (9,7) are shown in blue) and hexagons in Figure 2. This result suggests the diameter selectivity is around 1.17 nm in SWCNT growth. Next, PL spectroscopy was used to assign the (*n*,*m*) structure of semiconducting tubes. Figure 1c,d shows contour plots of the PL intensity collected from SWCNTs dispersed in 2 wt % sodium dodecyl benzene sulfonate (SDBS) $D_2O$ solution as a function of excitation and emission. The relative abundance of semiconducting (*n*,*m*) tubes identified in Figure 1c,d is determined by their PL intensities. Results are listed in Table S2 in the Supporting Information. Figure 1c and Table S2a show that the catalyst is highly selective to the single chiral (9,8) tube (51.7%) after 540 °C reduction. Several other (*n*,*m*) tubes (with relative abundance >3%) are also detectable in Figure 1c, such as (9,7), (10,6), (10,8), (8,7), (10,9), and (6,5). Similar to previous studies,[25−27] the existence of those species suggests a strong selectivity toward high chiral angle tubes in SWCNT growth. In contrast, the sample grown after 780 °C reduction comprises numbers of (*n*,*m*) tubes centered around (6,5) (16.3%) and (9,8) (17.5%).

To further evaluate the abundance of metallic tubes which cannot be observed in PL analysis, UV−vis−NIR absorbance spectrum of the sample produced after catalyst reduction at 540 °C is shown in Figure 3a. The label $E^S_{11}$ (shaded yellow) indicates the excitonic optical absorption bands for semiconducting SWCNTs corresponding to the first one-dimensional van Hove singularities; the $E^M_{11}$ and $E^S_{22}$ (shaded purple) correspond to the overlapping absorption bands of the first van Hove singularities from metallic SWCNTs and the second van Hove singularities from semiconducting SWCNTs. Intense absorption peaks at 1416 and 816 nm correspond to the first and second one-dimensional van Hove singularity transitions of (9,8) tubes. Additional absorption peaks below 700 nm may be assigned to either the $E^M_{11}$ transition of metallic tubes or $E^S_{22}$ transition of semiconducting tubes. We used a method based on the electron−phonon interaction model[44] to reconstruct the UV−vis−NIR absorbance spectrum

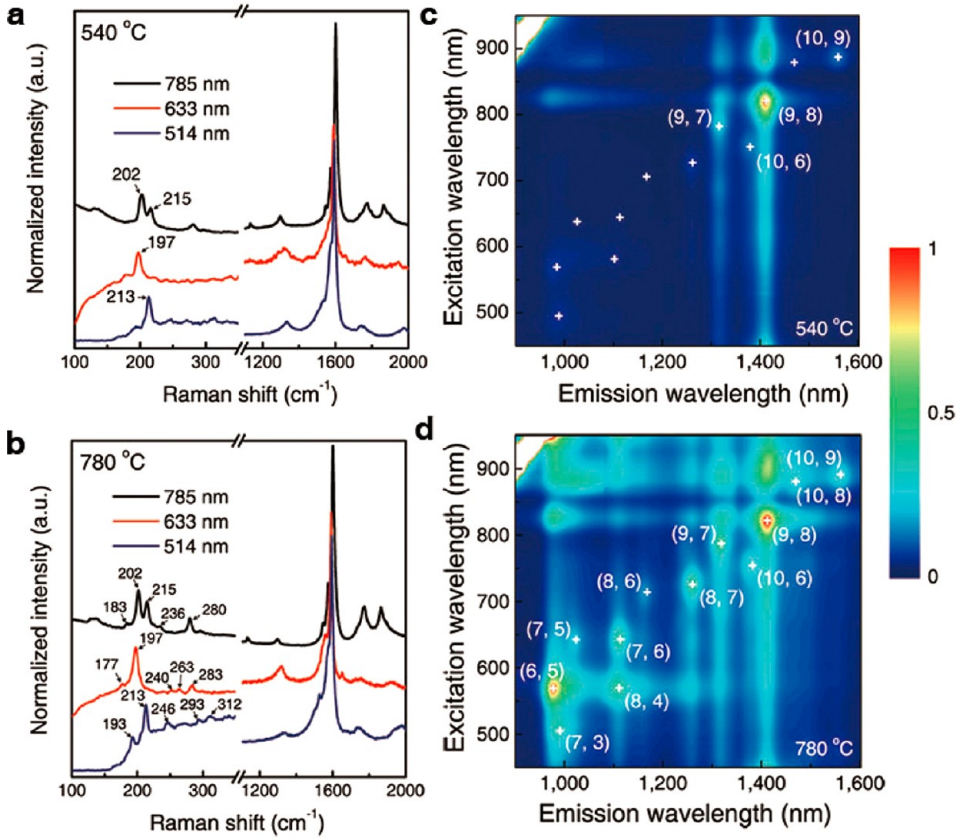


**Figure 1. (a,b) Raman spectra of SWCNTs under three excitation wavelengths for catalyst reduction at 540 and 780 °C, respectively. The regions on the left between 100 and 350 cm$^{-1}$ correspond to RBM peaks, while the regions on the right correspond to D and G bands. (c,d) PL contour plots as a function of excitation and emission energies from SDBS-dispersed SWCNTs grown after catalyst reduction at 540 and 780 °C, respectively. Major chiral tubes identified in PL are marked with their (*n*,*m*) indexes.**

(see Table S3 to S5 and detailed discussion in the Supporting Information). The thin Lorentzian peaks (black) in Figure 3b are from the contribution of individual semiconducting tubes, calculated by using the electron−phonon interaction model. Tubes with major contributions are marked with their (*n*,*m*) indexes. The thick solid line depicts the sum of all Lorentzian lines, and red circles are experimental data points. Figure 3c shows the $E_{11}^{M}$ and $E_{22}^{S}$ spectral reconstruction by the summation of the contribution from both semiconducting (black) and metallic (blue) SWCNTs. Other than (*n*,*m*) tubes identified in Raman and PL, Figure 3b,c shows a few additional peaks identified in absorption spectra, including semiconducting (12,4), (14,3), and (15,1) and metallic (9,6) and (10,10). Using the contribution from each (*n*,*m*) tube obtained in reconstructing the absorbance spectrum, their relative abundance of (*n*,*m*) tubes is shown in Figure 3d. It indicates that the dominant semiconducting tubes identified in PL have much higher abundance as compared to additional metallic tubes identified in absorption spectroscopy. Overall, the abundance of (9,8) tubes is 33.5%, followed by (9,7) at 7.1%. This further corroborates that the $CoSO_4/SiO_2$ catalyst is highly selective toward the (9,8) tube. The diameter of produced SWCNTs was also analyzed by TEM and AFM. As shown in Figure S5 in the Supporting Information, the diameter of 45% tubes among ∼100 measured ones is between 1.15 and 1.20 nm. Similarly, Figure S6 shows the height profiles of individual nanotubes deposited on the mica surface with a height of ∼1.2 nm. Both TEM and AFM results agree with spectroscopic results.

The carbon yield is an important criterion for evaluating catalysts used in SWCNT growth. It is necessary to achieve not only good chiral selectivity but also adequate nanotube yield so that scalable production process can be further developed. TGA was used to determine the yield of carbon species. Figure 4 shows the TG and differential TG (DTG) profiles of carbon deposits on catalysts after two reduction conditions. The total carbon yields (the weight loss between 200 and 1000 °C) are 3.8 and 3.5 wt % for the 540 and 780 °C reduction, respectively. The Co loading on the $SiO_2$ substrate is ∼1 wt %, thus the $CoSO_4/SiO_2$ catalyst has the carbon/metal ratio of 3.8. On the basis of the Raman spectroscopy results shown in Figure 1a, the dominant DTG peak at 560 °C in Figure 4a can be attributed to the oxidation of SWCNTs, which counts for more than 90% of the total carbon deposits based on the integrated peak areas. There are multiple DTG peaks of different carbon species in Figure 4b. The peak

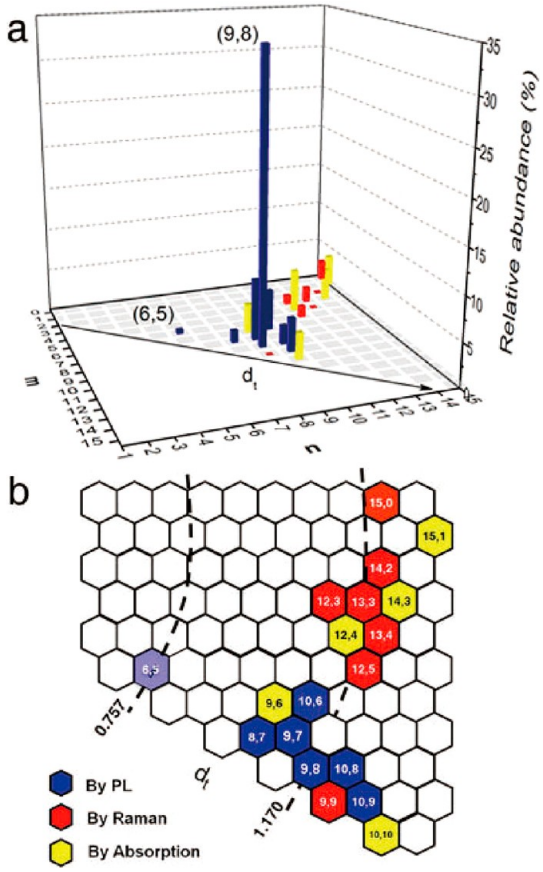


**Figure 2. (a) Relative abundance of (*n*,*m*) SWCNTs produced from the $CoSO_4/SiO_2$ catalyst after catalyst reduction at 540 °C. They are identified by the three characterization techniques. Blue, PL; red, Raman; yellow, absorption. (b) Two-dimensional projected chirality map of SWCNTs. Most of (*n*,*m*) species produced in the work are at larger diameter around 1.17 nm, as compared to previous chiral selectivity synthesis studies usually around 0.76 nm.**

around 300 °C can be credited to the oxidation of amorphous carbon. The peak at 520 °C is contributed by SWCNTs. The peak above 800 °C may come from the oxidation of graphite layers covering large Co particles. We compared the result in this work with a number of previous SWCNT chiral selectivity growth studies, as listed in Table S6 in the Supporting Information. Especially, compared to the Co-TUD-1 catalyst,[34] which has similar chiral selectivity toward (9,8) tubes, the carbon yield of the $CoSO_4/SiO_2$ catalyst is more than twice that of the Co-TUD-1 catalyst (1.5 wt %). Moreover, it would take 3 days to synthesize the Co-TUD-1 catalyst through aging, drying, and hydrothermal treatments, while the $CoSO_4/SiO_2$ catalyst can be produced by impregnation within 12 h. Overall, the $CoSO_4/SiO_2$ catalyst shows several advantages: first, it provides a unique single chiral selectivity toward a large diameter tube; second, this catalyst has an adequate SWCNT yield, which is important for scalable production of SWCNTs; and third, it is easy to synthesize, as compared to many mesoporous catalysts.

To better understand the $CoSO_4/SiO_2$ catalyst, we first characterized its morphology by SEM and TEM. Figure 5a shows that fresh catalyst is composed of small $SiO_2$ particles. Figure 5e indicates that the size of these solid $SiO_2$ particles is around 20 nm. They aggregate together to form a porous composite. After catalyst reduction at 540 °C and SWCNT growth, the catalyst shows no noticeable morphological changes (see Figure 5b,c). This is because the fumed $SiO_2$ particles are produced by the flame hydrolysis of chlorosilanes at high temperature, and they are usually stable after high-temperature treatments. Figure 5c shows a large amount of SWCNTs on the surface of aggregated $SiO_2$ particles. Figure 5f indicates that SWCNTs grow from Co particles on/in $SiO_2$ particles and aggregate together into small bundles of 10−20 nm in diameter. Very few Co particles can be easily observed in our TEM analysis of the catalysts after temperature was reduced to 540 °C or after SWCNT growth. We suspect that Co particles could be embedded under or near the surface of $SiO_2$ particles. This also suggests that Co species are well-dispersed on $SiO_2$ particles. After SWCNT growth, $SiO_2$ particles can be easily dissolved by refluxing in NaOH aqueous solution. Figure 5d shows dense SWCNT networks on filter paper after $SiO_2$ removal. We further characterized the physicochemical properties of the catalyst by XRD, nitrogen physisorption, UV−vis spectroscopy, and $H_2$-TPR. Figure 6a shows a broad diffraction peak near $2\theta = 21°$ originating from $SiO_2$ supports, suggesting the absence of Co oxides ($CoO_x$) or bulk Co silicates. Figure 6b shows that the catalyst is a porous material with a pore size around 32 nm. The pores are likely the gaps among $SiO_2$ particles in the catalyst aggregate. It has a surface area of 208 $m^2/g$ and a large pore volume of 1.54 mL/g. UV−vis spectra in Figure 6c designate the local environment of Co species on $SiO_2$. Similar to the pure $CoSO_4$, the catalyst shows a broad peak ascribed to the $^4T_{1g} \rightarrow {}^4T_{1g}(P)$ transition of octahedral $Co^{2+}$ ions. In contrast to $Co_3O_4$, the catalyst does not have absorption peaks at 410 and 710 nm. This is also different from the UV−vis spectrum of the Co-TUD-1 catalyst, which displays a minor peak shoulder at 660 nm and two broad peaks at 410 and 710 nm, pointing to the existence of tetrahedral $Co^{2+}$ and octahedral $Co^{3+}$ ions.[34,45] The $H_2$-TPR profile of the catalyst in Figure 6d shows a sharp reduction peak centered at 470 °C. This is different from common $CoO_x$ catalysts, which are usually reduced below 400 °C, as sketched by the two $CoO_x$ references (CoO and $Co_3O_4$). In comparison, pure $CoSO_4$ powder is reduced at 584 °C, suggesting that the reduction peak at 470 °C is credited to the reductive decomposition of highly dispersed $CoSO_4$. These results show that the $CoSO_4/SiO_2$ catalyst has unique physicochemical properties, as compared with other Co catalysts,[25,33] with a very narrow Co reduction window.

The narrow reduction window suggests that Co particles with a narrow size distribution may have been formed. Previous experimental and theoretical studies

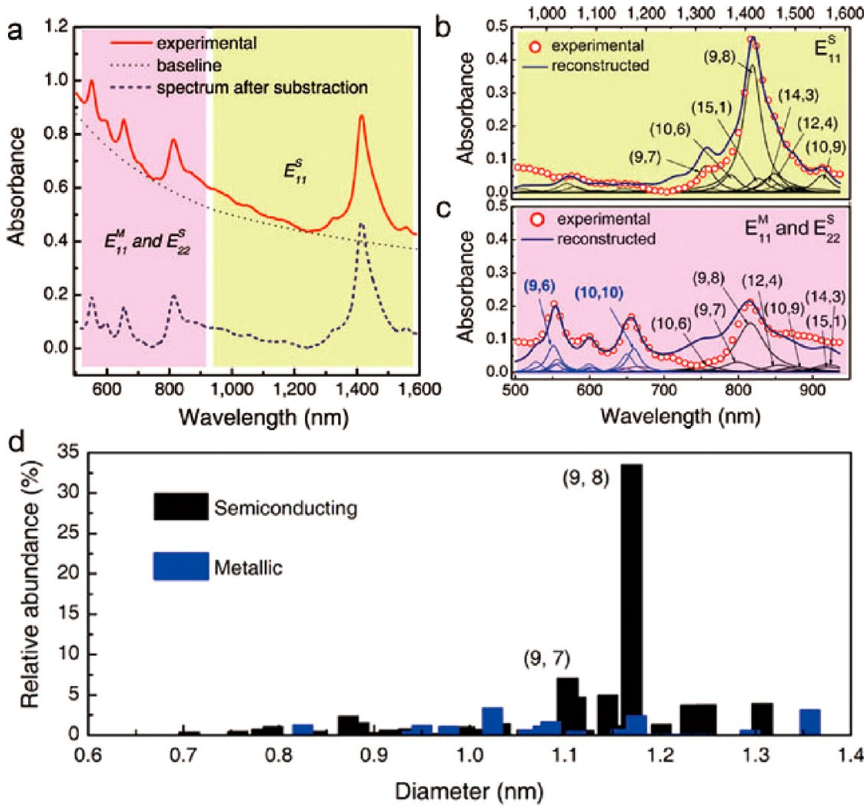


**Figure 3. (a) UV−vis−NIR absorbance spectra of SDBS-dispersed SWCNTs grown after catalyst reduction at 540 °C before and after baseline subtraction. (b) $E^S_{11}$ spectral reconstruction by the summation of the contribution from each (*n*,*m*) semiconducting SWCNT (Lorentzian peaks in black). (c) $E^M_{11}$ and $E^S_{22}$ spectral reconstruction by the summation of the contribution from both semiconducting (black) and metallic (blue) SWCNTs. The (*n*,*m*) indexes, thick solid line and red circles represent the same as in (b). (d) Relative abundance of both semiconducting (black) and metallic (blue) (*n*,*m*) SWCNTs obtained from the reconstruction of absorption spectra.**

predict a linear correlation between catalyst particle size and SWCNT diameter[19,46−48] with their ratio ranging from 1.1 to 1.6.[49] The (9,8) tubes at 1.17 nm produced after catalyst reduction at 540 °C suggest that catalytic particles have a narrow diameter distribution around 1.29−1.87 nm.[49] To verify this hypothesis, we investigated catalysts using XAS (see Methods for details). XAS was used here because most small Co particles are under the surface of $SiO_2$ particles, and it is difficult to quantify their diameters by TEM. The near-edge spectra (XANES) at the Co *K*-edge in Figure 7a show that Co atoms in the fresh catalyst are oxidized with a strong white line peak. After $H_2$ reduction and SWCNT growth, the white line is reduced together with the appearance of a strong pre-edge peak, showing the formation of metal Co particles. The extended X-ray absorption fine structure (EXAFS) of catalysts was Fourier transformed to *r*-space to separate the contribution from different coordination shells of Co atoms. Figure 7b shows that the fresh catalyst has a strong Co−O peak, while the reduced catalyst after SWCNT growth has an intense Co−Co peak. The spectrum in the *r*-space was fitted using paths of metallic Co generated by the FEFF 9 program[50] to obtain the first shell coordination number ($N_{Co-Co}$), listed in Table 1. The catalyst reduced at 540 °C after SWCNT growth has a $N_{Co-Co}$ of 7.04. The difference in bond distances with respect to the theoretical references (d*R*) is −0.016. The Debye−Waller factor ($\Delta\sigma^2$) is 0.007, indicating that the fit is within acceptable limits. The first shell coordination number of nanoparticles is a nonlinear function of particle size, which has been used to quantify the nanoparticle size. Using a (111)-truncated hemispherical cubic octahedron model,[51] Figure 7c shows that the average size of Co particles produced after catalyst reduction at 540 °C is 1.23 nm, which matches the diameter of (9,8) tubes.

An intriguing question is why the selectivity of the $CoSO_4/SiO_2$ catalyst is toward (9,8) tubes rather than some other chiral species? We emphasized the tentative nature of the following explanation on the chiral selectivity toward (9,8) tubes in the spirit of stimulating further exploration in understanding the chiral selection mechanism in SWCNT growth. Previous theoretical studies on the structure stability of $Ni_{2-55}$[52] and the electric dipole polarizability experimental study of $Ni_{12-58}$[53] and $Pt_n$ ($n$ = 13, 38, and 55)[54] showed that some nanoparticles with optimized structures are more stable than others. Using the method of previous studies,[55,56] we investigated the structure of Co particles and found that the optimized stable $Co_{13}$, $Co_{55}$,

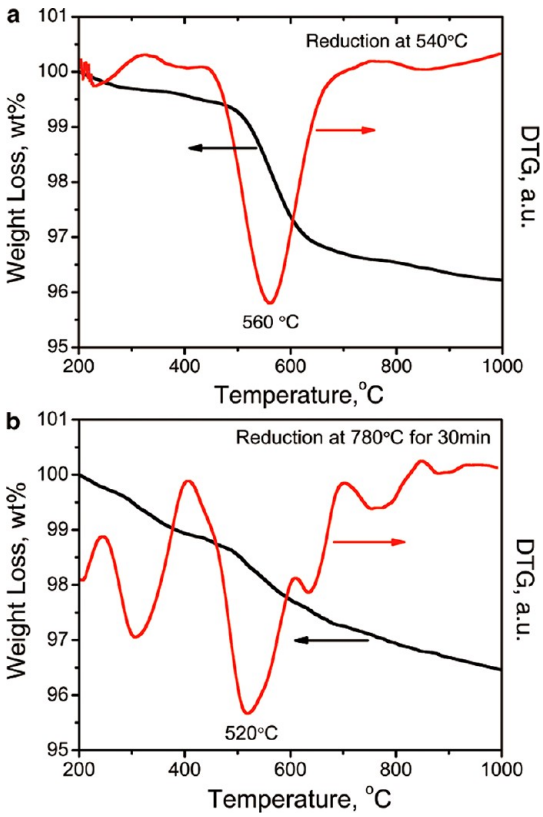


**Figure 4. TGA and DTG profiles of carbon deposits synthesized on the $CoSO_4/SiO_2$ catalyst. (a) Catalyst reduction at 540 °C, and then SWCNT growth at 780 °C, (b) reduction at 780 °C for 30 min, and then SWCNT growth. The total carbon yield is calculated from the weight loss between 200 and 1000 °C.**

and $Co_{147}$ particles adopt an icosahedral geometry (see Methods). The detailed calculated results, including the average binding energy $E_b$, bond lengths from the central Co atom $R_{Co\text{-}Cen}$, and surface bond lengths $R_{Co-Co}$, are listed in Table S7 in the Supporting Information. As sketched in Figure 7d, the stable $Co_{13}$ and $Co_{55}$ particles are comparable with carbon caps (cap 20 and cap (6,5)) at diameters of 6.2 and 8.3 Å, respectively. Very small SWCNTs extended from the "cap 20" are unstable. Thus, they are seldom found in SWCNT products. The (6,5) tube matching with the $Co_{55}$ is the most common species found in a number of (*n*,*m*)-selective synthesis studies.[25−27,29,33] By adding one complete atomic layer of Co atoms on the surface of $Co_{55}$, the $Co_{147}$ particle is more stable than other clusters in its diameter range. The cap (9,8) with a diameter of 11.55 Å fits well with the $Co_{147}$. There is a clear match between the most abundant (*n*,*m*) species (*i.e.*, (6,5) and (9,8)) and the stable Co particles (*i.e.*, $C_{55}$ and $Co_{147}$). The shift of (*n*,*m*) selectivity from the small-diameter (6,5) tube to the larger diameter (9,8) tube found in this study could be credited to the jump in the diameter of Co particles with optimized structures. We also noticed that many previous chirality-selective growth studies managed to tune (*n*,*m*) selectivity to some extent,[35−40] but none can achieve continuous changes of (*n*,*m*) selectivity over a wider diameter range. This suggests that matching with stable catalytic particles may be a fundamental requirement governing the growth of SWCNTs. It highlights that the efforts in achieving chiral-selective synthesis of SWCNTs should focus on growing chiral tubes with diameters similar to the most stable particles in their size range under growth conditions, other than seeking selectivity to random chiral structures. It should also be noted that adsorption and diffusion of carbon species during SWCNT growth can cause the reconstruction of catalytic particles,[57−59] which may also change the (*n*,*m*) selectivity to some extent. This may explain why tubes, such as (9,7), (10,6), and (10,9) near the main (9,8), are also produced. Moreover, the chiral angle-dependent growth rate[22,23] could also be the reason of growing the large chiral angle (9,8) tubes, rather than other (*n*,*m*) species at the same diameter with smaller chiral angles.

From the catalyst design perspective, a key task is to find out what components in the $CoSO_4/SiO_2$ catalyst are responsible for stabilizing Co particles which leads to the growth (9,8) tubes. Cobalt oxides ($CoO_x$) are usually reduced below 400 °C, leading to large Co particles, which are easily covered by graphite layers during SWCNT synthesis. On the other hand, Co incorporated in some mesoporous $SiO_2$ templates, such as MCM-41, or in cobalt silicates, is reduced at temperature above 700 °C.[60−62] They would form smaller Co particles, which are selective to smaller diameter tubes, such as (6,5) and (7,5). In our previous study of Co-TUD-1 catalyst,[34] we proposed that Co species on the mesoporous TUD-1 can nucleate in two steps. First, $Co^{2+}$ ions are partially reduced in $H_2$ during prereduction, but they are still dispersed in an isolated manner on the large surface of TUD-1. Second, Co atoms aggregate quickly into clusters under CO to initiate SWCNT growth. Co ions are incorporated into the amorphous silica walls of TUD-1, and the large surface area of TUD-1 and the strong metal−support interaction are sufficient in stabilizing these clusters with a narrow diameter distribution at around 1.2 nm, responsible for the growth of (9,8) nanotubes. However, the structure of the $CoSO_4/SiO_2$ catalyst is very different from the Co-TUD-1: first, Co ions cannot be incorporated into solid $SiO_2$ particles by the impregnation method; second, the surface area of the $CoSO_4/SiO_2$ catalyst is much smaller (208 $m^2/g$) as compared to TUD-1 (740 $m^2/g$). Thus, the way the $CoSO_4/SiO_2$ catalyst controls the formation of Co particles is expected to be different from that of the Co-TUD-1. We further tested different Co precursors in catalyst synthesis, including cobalt(II) nitrate, cobalt(II) acetate, cobalt(II) acetylacetonate, and cobalt(III) acetylacetonate. None of the above Co precursors deposited on $SiO_2$ particles showed good selectivity toward (9,8)

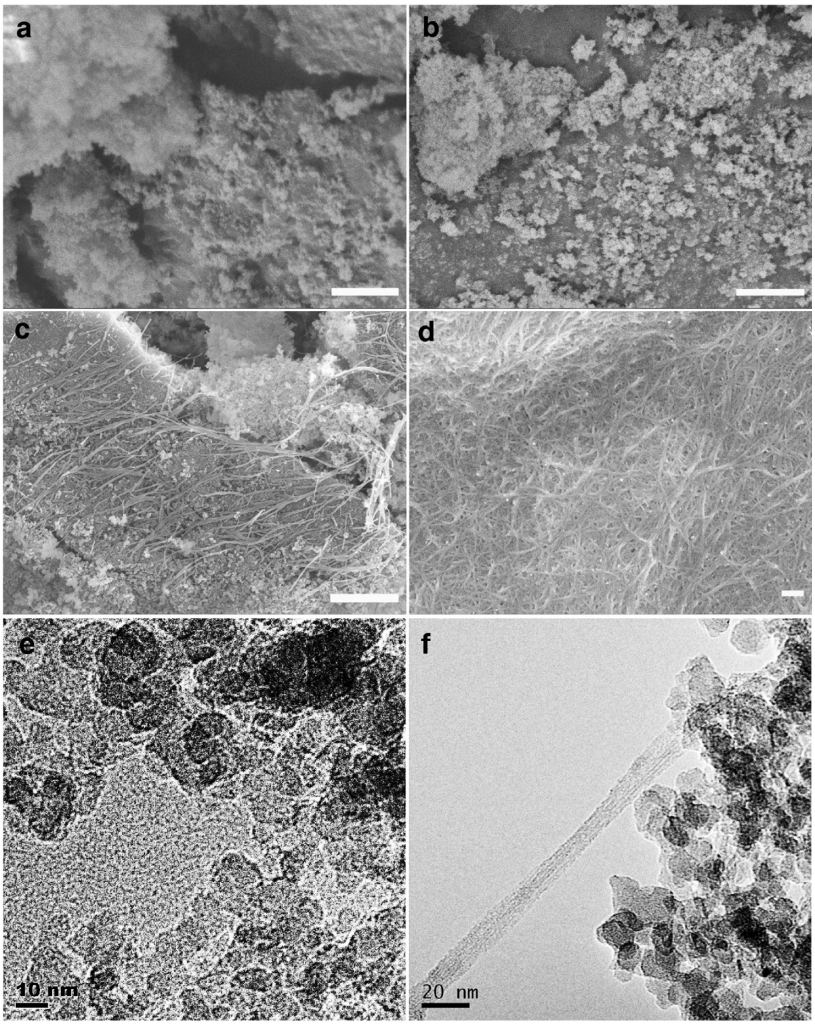


**Figure 5. SEM (a−d) and TEM (e,f) images of catalysts and SWCNTs. (a) fresh catalyst; (b) catalyst after reduction in $H_2$ at 540 °C, and then cooled to room temperature under He; (c) as-synthesized SWCNTs on catalyst; and (d) SWCNT films after $SiO_2$ removal. The scale bars in (a−c) are 1 $\mu$m and 100 nm in (d). (e) Same sample as (b), and (f) same sample as (c).**

tubes. Thus, we propose that the narrow reduction peak of the $CoSO_4/SiO_2$ catalyst at 470 °C can be credited to the reduction of highly dispersed $CoSO_4$, following the chemical reaction eqs 1 and 2. We used the reduction of $Co_3O_4$ and CoO (chemical reaction eqs 3 and 4) as references to quantify the $H_2$ consumption in $CoSO_4$ reduction on the $CoSO_4/SiO_2$ catalyst. Stoichiometric ratio of $H_2$ needed for reducing the same amount of Co ions in $CoSO_4$ over those in $Co_3O_4$ or CoO is 3.75−3 or 5−4, respectively. The integrated reduction peak area ratio between $CoSO_4$ and $Co_3O_4$ in Figure 6d is 3.68, and the ratio between $CoSO_4$ and CoO is 4.12. It is consistent with the proposed chemical reaction equations. Moreover, the existence of reaction eq 2 suggests that the presence of sulfur or $SO_4^{2-}$ ions is a contributing factor to stabilize Co particles on the $CoSO_4/SiO_2$ catalyst.

$$CoSO_4 + 5H_2 \rightarrow Co + H_2S + 4H_2O \quad (1)$$

$$CoSO_4 + 4H_2 \rightarrow CoS + 4H_2O \quad (2)$$

$$Co_3O_4 + 4H_2 \rightarrow 3Co + 4H_2O \quad (3)$$

$$CoO + H_2 \rightarrow Co + H_2O \quad (4)$$

Next, we verified the existence of sulfur compounds in the catalyst during SWCNT synthesis by XAS and elemental analysis. Figure 8a shows the XANES spectra at sulfur *K*-edge of catalysts after different treatments. The peak belonging to $SO_4^{2-}$ ions decreases with the increase of reduction temperature, and a small CoS peak can be observed. We quantified sulfur contents in catalysts by integrating the sulfur peak area of XANES spectra. Figure 8b shows that sulfur content decreases with increasing reduction temperature. This is further corroborated by element analysis of sulfur. The sulfur content in fresh catalyst is 0.65 wt %. After reduction at 540 °C, it drops to 0.36 wt %. In contrast, after reduction at 780 °C, catalyst only contains 0.11 wt % of sulfur. Figure 8, combining with the above SWCNT analysis, suggests that the sulfur content correlates with the (*n*,*m*) selectivity changes of the $CoSO_4/SiO_2$ catalyst.

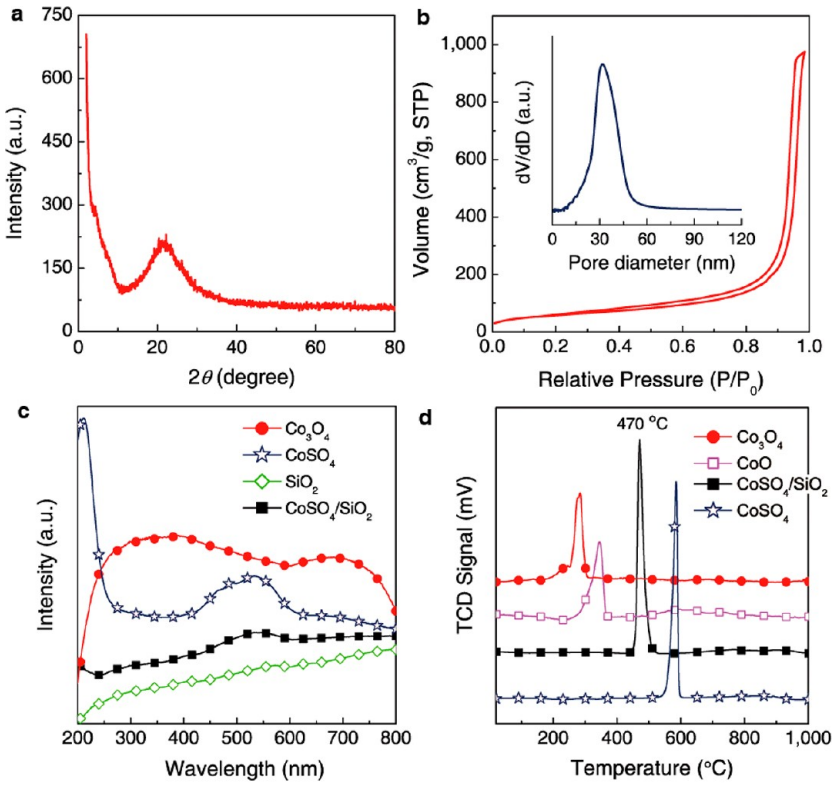


**Figure 6. Physicochemical properties of the $CoSO_4/SiO_2$ catalyst. (a) X-ray diffraction pattern of the calcined $CoSO_4/SiO_2$ catalyst. (b) Nitrogen physisorption isotherms and pore size distribution (inset) of the catalyst. (c) UV−vis absorption spectra of the catalyst and several references ($Co_3O_4$, $CoSO_4$ powders, and fumed $SiO_2$). (d) $H_2$ temperature-programmed reduction profiles of the catalyst and several Co references ($Co_3O_4$, CoO, and $CoSO_4$).**

From the TPR result in Figure 6d, the reduction of Co species under $H_2$ starts at 435 °C and completes at 530 °C. When catalyst is reduced at 540 °C, the existence of sulfur compounds may stabilize reduced Co atoms for forming Co particles with suitable diameter and composition under CO. Such particles lead to the selective growth of (9,8) tubes. In contrast, if the reduction temperature is further increased to 780 °C, sulfur compounds (*e.g.*, $SO_4^{2-}$ ions) are removed from the catalysts, and reduced Co atoms nucleate into Co particles with various diameters, leading to SWCNTs with a broader (*n*,*m*) distribution. The TGA result in Figure 4b shows the formation of amorphous carbon and graphite, resulting from Co particles of random sizes.

Previous studies showed that, when suitable amounts of sulfur are added in carbon precursors, it not only promotes the growth rate and the yield of carbon nanotubes but also strongly affects nanotube structures (such as shell number and diameter).[41,63−65] One study proposed a mechanism that sulfur (from thiophene or carbon disulfide added in gas phase) would restrict the growth of Fe particles at ~1.6 nm for chiral-selective growth of metallic (9,9) and (12,12) tubes.[66] They also suggested that sulfur may form C−S bonds at the edge steps of the nanotube growth front, which lowers the activation energy of Stone-Thrower-Wales dislocation motion for SWCNT growth.[66] In this study, sulfur compounds are directly impregnated on the catalyst instead, and the growth temperature at 780 °C is much lower than the previous study at 1200 °C.[66] Thus, the Co particles would not be in a liquid state during SWCNT growth. We propose that sulfur could play two roles: First, the coexistence of sulfur atoms near Co atoms may limit the aggregation of Co atoms, which does not happen on catalysts prepared using other Co precursors without sulfur. Second, sulfur atoms may also form various Co−S compounds on Co particles, as indicated by the small CoS peak in XAS results (Figure 8a). The Co−S compounds could enable the specific chiral selectivity different from pure Co particles. More studies are still ongoing in our lab to better understand the detailed roles of sulfur on stabilizing Co particles and the exact size, morphology, and composition of chirally selective Co particles.

## CONCLUSIONS

In this work, we show that the sulfate-promoted $CoSO_4/SiO_2$ catalyst is highly selective in growing large-diameter (9,8) SWCNTs. In contrast, the chiral selectivity reported by most previous studies is restricted to small-diameter (6,5) and (7,5) SWCNTs. After the catalyst is reduced in $H_2$ at 540 °C, it grows 51.7% (by PL, 33.5% by absorption) of (9,8) tubes. The total carbon yield over all catalyst materials used is 3.8 wt %, in which at least 90% is SWCNTs. The selectivity toward

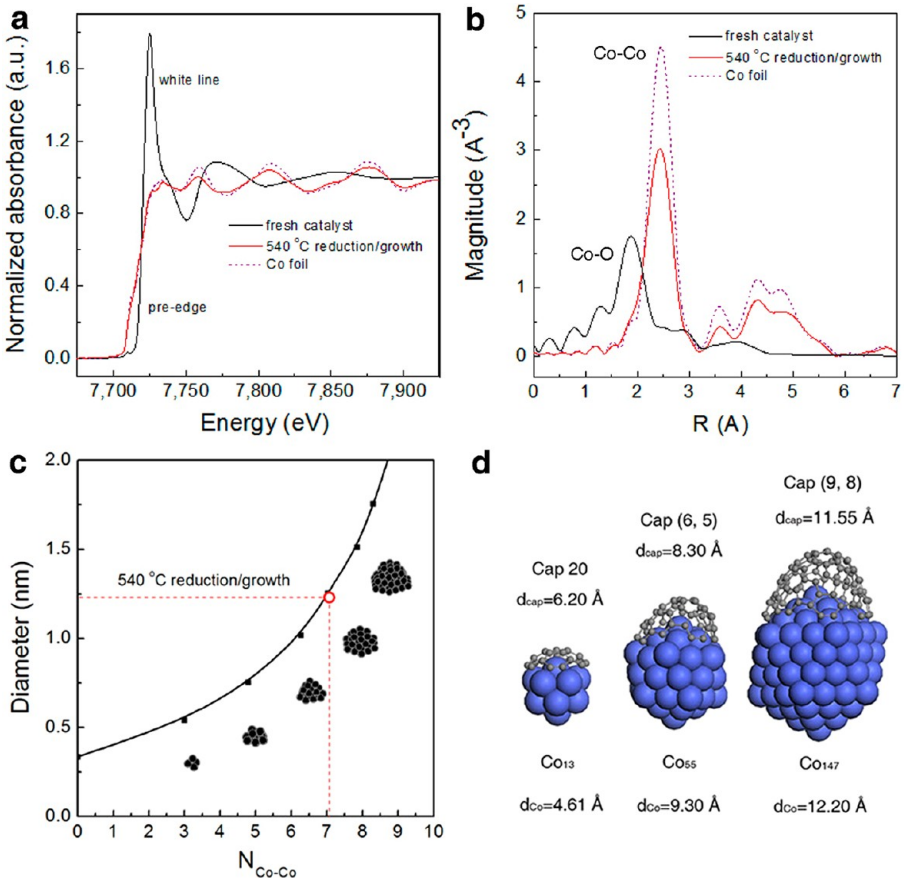


**Figure 7. XAS spectra of the $CoSO_4/SiO_2$ catalysts and model of Co clusters. (a) Near-edge spectra at the Co *K*-edge ($E_0$ = 7709 eV) of fresh catalyst, catalysts after reduction at 540 °C and SWCNT growth, and Co foil. (b) Fourier transform of EXAFS spectra at the Co *K*-edge for samples in (a). (c) Average diameter of Co metal clusters in catalysts determined by the first shell coordination number from XAS spectra. (d) Optimized structures of $Co_n$ (*n* = 13, 55, and 147) clusters from theoretical simulation and their likely matching carbon caps.**

**TABLE 1. Structure Parameters of the First Co–Co Coordination Shell in Catalyst Determined from the EXAFS Data (Figure 7b) at the Co *K*-Edge by Fitting Using FEFF 9**

| | Co–Co first shell fitting results | | |
|---|---|---|---|
| catalyst | $N_{Co-Co}$ | d*R* (Å) | $\Delta\sigma^2$ |
| 540 °C | 7.04 ± 0.86 | −0.016 ± 0.007 | 0.007 |

(9,8) tubes disappears if the catalyst is reduced at 780 °C. The uniqueness of the $CoSO_4/SiO_2$ catalyst is that the highly dispersed $CoSO_4$ is reduced in a narrow window near 470 °C. XAS results indicate the formation of Co particles with average size of 1.23 nm, matching the diameter of (9,8) tubes. Experimental and theoretical results suggest a correlation between the most abundant (*n*,*m*) species and the stable Co particles of scattered sizes. This suggests that growing chiral tubes with diameters matching the most stable particles in their size range could be much easier than seeking selectivity to random chiral structures. Furthermore, XAS results show that the sulfur content in the catalyst changes after catalyst reduction at different conditions, which correlates with the (*n*,*m*) selectivity change observed. Sulfur compounds incorporated in catalyst preparation may help to limit the aggregation of Co atoms and/or form various Co–S compounds, which contributes to the chiral selectivity. We expect that more novel catalysts incorporated with sulfur compounds will be developed to achieve chirally selective growth of SWCNTs.

## METHODS

**Catalyst Preparation.** The $CoSO_4/SiO_2$ catalyst was prepared by the incipient wetness impregnation method, in which metal salt dissolved in water is added to the catalyst support materials. Cobalt(II) sulfate heptahydrate (Sigma-Aldrich, ≥99% purity) was first dissolved in deionized water and then added to CAB-O-SIL M-5 fumed silica with a surface area of 254 $m^2/g$ and a pore volume of 0.89 mL/g. The total Co weight loading in the catalyst is ~1.0 wt %. The mixture was first aged at room temperature for 1 h and afterward dried in an oven at 100 °C for 2 h. The dried catalyst was further calcined under airflow of 20 sccm per gram of catalyst from room temperature to 400 °C at 1 °C/min ramping rate and then kept at 400 °C for 1 h.

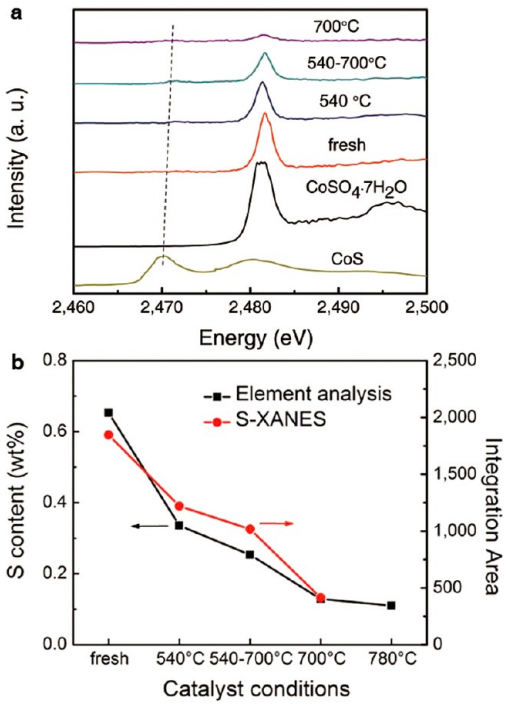


**Figure 8. Sulfur content in $CoSO_4/SiO_2$ catalyst. (a) XANES spectra at the sulfur *K*-edge of fresh and treated catalysts at different reduction conditions. $CoSO_4 \cdot 7H_2O$ and CoS are references. Four samples include (1) fresh catalyst; (2) catalyst reduced in $H_2$ at 540 °C, and then cooled to room temperature under He; (3) catalyst reduced in $H_2$ at 540 °C, and then increased temperature to 700 °C under He before cooled to room temperature; and (4) catalyst reduced in $H_2$ at 700 °C, and then cooled to room temperature under He. (b) Sulfur content in catalyst determined by element analysis and integrated sulfur peak area of XANES spectra. Four samples are the same as (a) and one more sample after reduction in $H_2$ at 780 °C.**

**SWCNT Synthesis.** To catalyze SWCNT growth, 200 mg of the $CoSO_4/SiO_2$ catalyst was loaded in a ceramic boat at the center of a horizontal chemical vapor deposition reactor. The catalyst was first reduced under pure $H_2$ (1 bar, 50 sccm, 99.99% from Alphagaz, Soxal), during which the reactor temperature was increased from room temperature to an elevated temperature at 20 °C/min. Once the reduction temperature reached 540 °C, the reactor was purged by Ar (99.99% from Alphagaz, Soxal), while its temperature was further increased to 780 °C. At 780 °C, pressured CO (6 bar, 99.9% from Alphagaz, Soxal) was introduced into the reactor at 200 sccm flow rate to initiate SWCNT growth, and the growth time was 1 h. Carbonyl residues in CO gas were removed by a purifier (Nanochem, Matheson Gas Products) before entering the reactor. In another experiment, the catalyst was reduced in $H_2$ from room temperature to 780 °C and further reduced for 30 min at 780 °C before exposing to CO.

**SWCNT Characterization.** As-synthesized SWCNTs deposited on the $CoSO_4/SiO_2$ catalyst were first studied by Raman spectroscopy. Raman spectra were collected with a Renishaw Ramanscope in the backscattering configuration over a few random spots on samples under 514, 633, and 785 nm lasers with the integration time of 10 s. Laser energies of 2.5−5 mW were used to prevent sample damages during the measurement. SWCNTs were further refluxed in 1.5 mol/L NaOH aqueous solution to dissolve the $SiO_2$ catalyst and then filtered on a nylon membrane (0.2 $\mu$m pores). We found no significant differences between the Raman spectra of as-synthesized SWCNTs and SWCNTs on filter membranes after catalyst removal. To obtain SWCNT suspensions, carbon deposits on filter membranes were further dispersed in 2 wt % SDBS (Aldrich) $D_2O$ (99.9 atom % D, Sigma-Aldrich) solution by sonication in a cup-horn ultrasonicator (SONICS, VCX-130) at 20 W for 1 h. After sonication, SWCNT suspensions were centrifuged for 1 h at 50 000*g*. SWCNT suspensions obtained after centrifugation were characterized by PL and absorption spectroscopy. PL was conducted on a Jobin-Yvon Nanolog-3 spectrofluorometer with the excitation scanned from 450 to 950 nm and the emission collected from 900 to 1600 nm. The UV−vis−NIR absorption spectra were measured from 500 to 1600 nm on the Varian Cary 5000 spectrophotometer. TGA was used to determine the yield of carbon species. As-synthesized SWCNTs together with catalyst substrates were characterized in TGA using a PerkinElmer Diamond TG/DTA Instruments. In a typical TGA, about 2 mg of the sample was loaded in an alumina pan. The sample was first heated to 200 °C and held at 200 °C for 10 min under airflow (200 sccm) to remove moisture. Afterward, its temperature was continuously increased from 200 to 1000 °C at a 10 °C/min rate. The weight loss of the sample was monitored and recorded as a function of the temperature. The same procedure was repeated after the sample was cooled to room temperature to obtain the second weight−temperature curve for baseline correction. The diameter of SWCNTs was also analyzed by TEM and AFM. TEM images of as-synthesized SWCNTs were recorded on a Philips Tecnai 12 microscope. SWCNT suspensions were drop-cast on mica surfaces to form nanotube networks. AFM images of nanotubes were recorded on a MFP3D microscope (Asylum Research, Santa Barbara, CA) with a cantilever (Arrow NC, Nanoworld) operating in the tapping mode.

**Catalyst Characterization.** The morphology, physical, and chemical properties of the $CoSO_4/SiO_2$ catalyst were evaluated by SEM, TEM, XRD, nitrogen physisorption, UV−vis diffuse reflectance spectroscopy, $H_2$-TPR, and element analysis. SEM images were obtained by using JEOL field-emission SEM (JSM-6701F) at 5 kV. TEM images were recorded on the Philips Tecnai 12 microscope. The solid samples were first dispersed in anhydrous ethanol by bath sonication for 30 min, and then one drop of the suspension was applied to a TEM grid covered with holey carbon film. XRD measurement of $CoSO_4/SiO_2$ catalyst powders was carried out on a Bruker Axs D8 X-ray diffractometer (Cu K$\alpha$, $\lambda = 0.15$, 4 nm, 40 kV, 30 mA). Nitrogen adsorption−desorption isotherms of the catalyst were measured at 77 K using a Quantachrome Autosorb-6b static volumetric instrument. Prior to the physisorption analysis, samples were degassed at 250 °C under high vacuum (<0.01 mbar). The specific surface area was calculated by the Brunauer, Emmet, and Teller (BET) method. The pore size and pore size distribution were calculated by the Barrett, Joyner, and Halenda (BJH) method using the desorption branch of the isotherms. UV−vis diffuse reflectance spectra of the $CoSO_4/SiO_2$ catalyst and several references, such as $Co_3O_4$ (Aldrich), $CoSO_4$ (Aldrich), and fumed silica ($SiO_2$), were recorded on the Varian Cary 5000 spectrophotometer. The samples were first dried at 100 °C for 3 h, and then UV−vis spectra were recorded in the range of 200−800 nm with $BaSO_4$ as a reference. The reducibility of calcined catalysts was characterized by $H_2$-TPR equipped with a thermal conductivity detector (TCD) of a gas chromatography (Techcomp 7900). Two-hundred milligrams of the catalyst or reference samples with equivalent Co loadings was loaded into a quartz cell. CoO, $Co_3O_4$, and $CoSO_4$ (Sigma-Aldrich) were used as reference samples in TPR analysis. $H_2$ (5%) in Ar was introduced to the quartz cell at 30 sccm. Pure Ar gas was used as a reference for the TCD. After the TCD baseline was stable, the temperature of the quartz cell was increased to 950 °C at 5 °C/min and then held at 950 °C for 30 min. An acetone−liquid $N_2$ trap was installed between the quartz cell and the TCD to condense water or $H_2S$ produced during the catalyst reduction. The weight concentration of sulfur in the catalysts at different reduction conditions was determined by an Elementarvario CHN elemental analyzer. Around 5 mg of each treated catalyst was used for each test, and at least three samples from each treatment condition were measured to obtain the mean value.

**XAS Characterization and Analysis.** The XAS spectra at the Co *K*-edge were recorded at the Beamline X18B at Brookhaven National Laboratory, USA. Three *ex situ* samples were measured, including the fresh $CoSO_4/SiO_2$ catalyst, the catalyst after SWCNT growth by reduction at 540 °C, and a Co metal foil. For catalyst

samples, catalyst fine powder was pressed at ~2 tons into a round self-supporting wafer (1.5 cm in diameter) using a hydraulic pellet press to reach the optimum absorption thickness ($\Delta\mu x \approx 1.0$, $\Delta\mu$ is the absorption edge, $x$ is the thickness of the catalyst wafer). Spectra were collected in a transmission mode at room temperature by scanning from 200 below to 1000 eV above the Co *K*-edge using gas-filled ionization chamber detectors. The monochromator of this beamline was a double-crystal Si(111) with an energy resolution of approximately 0.2 eV. The XANES spectra at the sulfur *K*-edge were recorded at the Beamline X15B. Four catalyst samples after different treatment conditions were measured. $CoSO_4 \cdot 7H_2O$ and CoS were used as references. The sample powder was brushed onto a thin strip of sulfur-free kapton tape, uncovered, facing the beam at 45°. Spectra were collected in a fluorescence mode at room temperature with the energy range of 2460−2500 eV with the step of 0.2 eV. Pure sulfur was used to calibrate the Si(111) monochromator.

The XAS experimental data at the Co *K*-edge were analyzed using the IFEFFIT program[50] in three steps. (1) The XAS function ($\chi$) was obtained by subtracting the post-edge background, and then normalized with respect to the edge jump step. (2) The normalized $\chi(E)$ was transferred from energy space to photoelectron wave vector *k*-space. The $\chi(k)$ data were multiplied by $k^2$ to compensate for the damping of oscillations in the high *k*-region. Then the $k^2$-weighted $\chi(k)$ data in *k*-space ranging from 2 to 12.5 $Å^{-1}$ for the Co *K*-edge were Fourier transformed to *r*-space to separate the contribution from the different coordination shells. (3) The spectra in the *r*-space between 1.1 and 3.35 Å were fitted using paths of metallic Co generated by the FEFF 9 to obtain parameters, including the first shell coordination number ($N_{Co-Co}$), bond distance ($R$), and the Debye−Waller factor ($\Delta\sigma^2$).

**Simulation of $Co_n$ Particles.** The structures of a series of $Co_n$ ($n$ = 2, 3, 5, 13, 55, and 147) particles were fully relaxed to optimize without any constraint. All spin-polarized computations were performed with the Perdew−Burke−Ernzerhof (PBE) exchange correlation function[67] using the VASP code.[68,69] The interaction between an atomic core and electrons was described by the projector-augmented wave method.[70,71] The plane-wave basis set energy cutoff was set to 400 eV. Periodic boundary conditions were implemented with at least 1 nm vacuum to preclude interactions between a cluster and its images. Simulation boxes were 22 × 22 × *C* Å (where *C* is from 20 to 24 Å) for different calculated systems. The reciprocal space integration was performed with a 1 × 1 × 1 *k*-point mesh for all calculated systems with discrete characters. On the basis of previous studies,[55,56] Co particles with icosahedral structures are lower in energy than other structures. $Co_{13}$, $Co_{55}$, and $Co_{147}$ adopt the icosahedral geometry. $Co_{13}$ has one atom at the center and the other 12 identical atoms on the spherical shell surface with a coordination number of 6. The distance between the spherical shell and the central atom is 2.32 Å. The surface bond length is 2.44 Å. From the $Co_{13}$ icosahedral structure, the $Co_{55}$ was built by adding 30 atoms on the edge atoms of $Co_{13}$ with a coordination of 8, and additional 12 atoms on the vertex atoms of $Co_{13}$ with a coordination number of 6. Using the same methodology, $Co_{147}$ was built by adding 80 atoms on the edge atoms of $Co_{55}$ with a coordination of 8, and additional 12 atoms on the vertex atoms of $Co_{55}$ with a coordination number of 6. Their diameters successively increase from ~0.46 to ~0.93 and 1.22 nm, respectively. The geometrical structure of these three clusters is illustrated in Figure 7d. $Co_2$, $Co_3$, $Co_5$ clusters, and Co-bulk has also been calculated as references.

*Conflict of Interest:* The authors declare the following competing financial interest(s): A technical disclosure has been filed by Nanyang Technological University.

*Acknowledgment.* This work was supported by National Research Foundation, Singapore (Grant No. NRF-CRP2-2007-02) and Ministry of Education, Singapore (MOE2011-T2-2-062). Use of beamlines at the National Synchrotron Light Source, Brookhaven National Laboratory, was supported by the U.S. Department of Energy, Office of Science, Office of Basic Energy Sciences, under Contract No. DE-AC02-98CH10886. We acknowledge Ms. Changchang Liu and Dr. Paul Northrup for support with collecting the XAS data.

*Supporting Information Available:* Analysis of RBM peaks, relative abundance of (*n*,*m*) tubes, reconstruction of absorbance spectra, SWCNT diameter analysis by TEM and AFM, comparison of (*n*,*m*) selectivity and carbon yield among several reported chiral-selective growth studies, and spin-polarized density functional study of stable Co clusters. This material is available free of charge *via* the Internet at http://pubs.acs.org.

## REFERENCES AND NOTES

1. Baughman, R. H.; Zakhidov, A. A.; de Heer, W. A. Carbon Nanotubes—The Route toward Applications. *Science* **2002**, *297*, 787–792.
2. Jorio, A.; Dresselhaus, G.; Dresselhaus, M. S. *Carbon Nanotubes, Advanced Topics in the Synthesis, Structure, Properties and Applications*; Springer: Berlin, 2008.
3. Tu, X. M.; Manohar, S.; Jagota, A.; Zheng, M. DNA Sequence Motifs for Structure-Specific Recognition and Separation of Carbon Nanotubes. *Nature* **2009**, *460*, 250–253.
4. Arnold, M. S.; Green, A. A.; Hulvat, J. F.; Stupp, S. I.; Hersam, M. C. Sorting Carbon Nanotubes by Electronic Structure Using Density Differentiation. *Nat. Nanotechnol.* **2006**, *1*, 60–65.
5. Liu, H. P.; Nishide, D.; Tanaka, T.; Kataura, H. Large-Scale Single-Chirality Separation of Single-Wall Carbon Nanotubes by Simple Gel Chromatography. *Nat. Commun.* **2011**, *2*, 309.
6. Wei, L.; Lee, C. W.; Li, L. J.; Sudibya, H. G.; Wang, B.; Chen, L. Q.; Chen, P.; Yang, Y. H.; Chan-Park, M. B.; Chen, Y. Assessment of (*n*,*m*) Selectively Enriched Small Diameter Single-Walled Carbon Nanotubes by Density Differentiation from Cobalt-Incorporated MCM-41 for Macroelectronics. *Chem. Mater.* **2008**, *20*, 7417–7424.
7. Lamouroux, E.; Serp, P.; Kalck, P. Catalytic Routes towards Single Wall Carbon Nanotubes. *Catal. Rev.* **2007**, *49*, 341–405.
8. Charlier, J. C.; DeVita, A.; Blase, X.; Car, R. Microscopic Growth Mechanisms for Carbon Nanotubes. *Science* **1997**, *275*, 646–649.
9. Kwon, Y. K.; Lee, Y. H.; Kim, S. G.; Jund, P. Morphology and Stability of Growing Multiwall Carbon Nanotubes. *Phys. Rev. Lett.* **1997**, *79*, 2065–2068.
10. Irle, S.; Ohta, Y.; Okamoto, Y.; Page, A. J.; Wang, Y.; Morokuma, K. Milestones in Molecular Dynamics Simulations of Single-Walled Carbon Nanotube Formation: A Brief Critical Review. *Nano Res.* **2009**, *2*, 755–767.
11. Shibuta, Y. A Numerical Approach to the Metal-Catalyzed Growth Process of Carbon Nanotubes. *Diamond Relat. Mater.* **2011**, *20*, 334–338.
12. Yuan, Q.; Xu, Z.; Yakobson, B. I.; Ding, F. Efficient Defect Healing in Catalytic Carbon Nanotube Growth. *Phys. Rev. Lett.* **2012**, *108*, 245505.
13. Gómez-Gualdrón, D. A.; Balbuena, P. B. The Role of Cap Chirality in the Mechanism of Growth of Single-Wall Carbon Nanotubes. *Nanotechnology* **2008**, *19*, 485604.
14. Dumlich, H.; Reich, S. Chirality-Dependent Growth Rate of Carbon Nanotubes: A Theoretical Study. *Phys. Rev. B: Condens. Matter Mater. Phys.* **2010**, *82*, 085421.
15. Gómez-Gualdrón, D. A.; McKenzie, G. D.; Alvarado, J. F. J.; Balbuena, P. B. Dynamic Evolution of Supported Metal Nanocatalyst/Carbon Structure during Single-Walled Carbon Nanotube Growth. *ACS Nano* **2012**, *6*, 720–735.
16. Gómez-Gualdrón, D. A.; Zhao, J.; Balbuena, P. B. Nanocatalyst Structure as a Template To Define Chirality of Nascent Single-Walled Carbon Nanotubes. *J. Chem. Phys.* **2011**, *134*, 014705.
17. Neyts, E. C.; van Duin, A. C. T.; Bogaerts, A. Changing Chirality during Single-Walled Carbon Nanotube Growth: A Reactive Molecular Dynamics/Monte Carlo Study. *J. Am. Chem. Soc.* **2011**, *133*, 17225–17231.
18. Diarra, M.; Amara, H.; Bichara, C.; Ducastelle, F. Role of Defect Healing on the Chirality of Single-Wall Carbon Nanotubes. *Phys. Rev. B: Condens. Matter Mater. Phys.* **2012**, *85*, 245446.
19. Fiawoo, M. F. C.; Bonnot, A. M.; Amara, H.; Bichara, C.; Thibault-Pénisson, J.; Loiseau, A. Evidence of Correlation

between Catalyst Particles and the Single-Wall Carbon Nanotube Diameter: A First Step towards Chirality Control. *Phys. Rev. Lett.* **2012**, *108*, 195503.
20. Reich, S.; Li, L.; Robertson, J. Control the Chirality of Carbon Nanotubes by Epitaxial Growth. *Chem. Phys. Lett.* **2006**, *421*, 469–472.
21. Dutta, D.; Chiang, W. H.; Mohan Sankaran, R.; Bhethanabotla, V. R. Epitaxial Nucleation Model for Chiral-Selective Growth of Single-Walled Carbon Nanotubes on Bimetallic Catalyst Surfaces. *Carbon* **2012**, *50*, 3766–3773.
22. Ding, F.; Harutyunyan, A. R.; Yakobson, B. I. Dislocation Theory of Chirality-Controlled Nanotube Growth. *Proc. Natl. Acad. Sci. U.S.A.* **2009**, *106*, 2506–2509.
23. Rao, R.; Liptak, D.; Cherukuri, T.; Yakobson, B. I.; Maruyama, B. *In Situ* Evidence for Chirality-Dependent Growth Rates of Individual Carbon Nanotubes. *Nat. Mater.* **2012**, *11*, 213–216.
24. He, M. S.; Jiang, H.; Kauppinen, E. I.; Lehtonen, J. Diameter and Chiral Angle Distribution Dependencies on the Carbon Precursors in Surface-Grown Single-Walled Carbon Nanotubes. *Nanoscale* **2012**, *4*, 7394–7398.
25. Bachilo, S. M.; Balzano, L.; Herrera, J. E.; Pompeo, F.; Resasco, D. E.; Weisman, R. B. Narrow (*n,m*)-Distribution of Single-Walled Carbon Nanotubes Grown Using a Solid Supported Catalyst. *J. Am. Chem. Soc.* **2003**, *125*, 11186–11187.
26. Maruyama, S.; Kojima, R.; Miyauchi, Y.; Chiashi, S.; Kohno, M. Low-Temperature Synthesis of High-Purity Single-Walled Carbon Nanotubes from Alcohol. *Chem. Phys. Lett.* **2002**, *360*, 229–234.
27. Li, X.; Tu, X.; Zaric, S.; Welsher, K.; Seo, W. S.; Zhao, W.; Dai, H. Selective Synthesis Combined with Chemical Separation of Single-Walled Carbon Nanotubes for Chirality Selection. *J. Am. Chem. Soc.* **2007**, *129*, 15770–15771.
28. Chiang, W. H.; Sankaran, R. M. Linking Catalyst Composition to Chirality Distributions of As-Grown Single-Walled Carbon Nanotubes by Tuning $Ni_xFe_{1-x}$ Nanoparticles. *Nat. Mater.* **2009**, *8*, 882–886.
29. He, M.; Chernov, A. I.; Fedotov, P. V.; Obraztsova, E. D.; Sainio, J.; Rikkinen, E.; Jiang, H.; Zhu, Z.; Tian, Y.; Kauppinen, E. I. Predominant (6,5) Single-Walled Carbon Nanotube Growth on a Copper-Promoted Iron Catalyst. *J. Am. Chem. Soc.* **2010**, *132*, 13994–13996.
30. Liu, B.; Ren, W.; Li, S.; Liu, C.; Cheng, H. M. High Temperature Selective Growth of Single-Walled Carbon Nanotubes with a Narrow Chirality Distribution from CoPt Bimetallic Catalyst. *Chem. Commun.* **2012**, *48*, 2409–2411.
31. Fouquet, M.; Bayer, B.; Esconjauregui, S.; Blume, R.; Warner, J.; Hofmann, S.; Schlögl, R.; Thomsen, C.; Robertson, J. Highly Chiral-Selective Growth of Single-Walled Carbon Nanotubes with a Simple Monometallic Co Catalyst. *Phys. Rev. B: Condens. Matter Mater. Phys.* **2012**, *85*, 235411.
32. Chen, Y.; Ciuparu, D.; Yang, Y. H.; Lim, S.; Wang, C.; Haller, G. L.; Pfefferle, L. D. Single-Wall Carbon Nanotube Synthesis by CO Disproportionation on Nickel-Incorporated MCM-41. *Nanotechnology* **2005**, *16*, S476–S483.
33. Chen, Y.; Ciuparu, D.; Lim, S.; Haller, G. L.; Pfefferle, L. D. The Effect of the Cobalt Loading on the Growth of Single Wall Carbon Nanotubes by CO Disproportionation on Co-MCM-41 Catalysts. *Carbon* **2006**, *44*, 67–78.
34. Wang, H.; Wang, B.; Quek, X.; Wei, L.; Zhao, J.; Li, L.; Chan-Park, M.; Yang, Y.; Chen, Y. Selective Synthesis of (9,8) Single Walled Carbon Nanotubes on Cobalt Incorporated TUD-1 Catalysts. *J. Am. Chem. Soc.* **2010**, *132*, 16747–16749.
35. Miyauchi, Y.; Chiashi, S.; Murakami, Y.; Hayashida, Y.; Maruyama, S. Fluorescence Spectroscopy of Single-Walled Carbon Nanotubes Synthesized from Alcohol. *Chem. Phys. Lett.* **2004**, *387*, 198–203.
36. Lolli, G.; Zhang, L.; Balzano, L.; Sakulchaicharoen, N.; Tan, Y.; Resasco, D. E. Tailoring (*n,m*) Structure of Single-Walled Carbon Nanotubes by Modifying Reaction Conditions and the Nature of the Support of CoMo Catalysts. *J. Phys. Chem. B* **2006**, *110*, 2108–2115.
37. Wang, B.; Yang, Y.; Li, L. J.; Chen, Y. Effect of Different Catalyst Supports on the (*n,m*) Selective Growth of Single-Walled Carbon Nanotube from Co−Mo Catalyst. *J. Mater. Sci.* **2009**, *44*, 3285–3295.
38. Wang, B.; Poa, C. H. P.; Wei, L.; Li, L. J.; Yang, Y.; Chen, Y. (*n,m*) Selectivity of Single-Walled Carbon Nanotubes by Different Carbon Precursors on Co−Mo Catalysts. *J. Am. Chem. Soc.* **2007**, *129*, 9014–9019.
39. Wang, B.; Wei, L.; Yao, L.; Li, L. J.; Yang, Y. H.; Chen, Y. Pressure-Induced Single-Walled Carbon Nanotube (*n,m*) Selectivity on Co−Mo Catalysts. *J. Phys. Chem. C* **2007**, *111*, 14612–14616.
40. Ishigami, N.; Ago, H.; Imamoto, K.; Tsuji, M.; Iakoubovskii, K.; Minami, N. Crystal Plane Dependent Growth of Aligned Single-Walled Carbon Nanotubes on Sapphire. *J. Am. Chem. Soc.* **2008**, *130*, 9918–9924.
41. Yu, B.; Liu, C.; Hou, P. X.; Tian, Y.; Li, S.; Liu, B.; Li, F.; Kauppinen, E. I.; Cheng, H. M. Bulk Synthesis of Large Diameter Semiconducting Single-Walled Carbon Nanotubes by Oxygen-Assisted Floating Catalyst Chemical Vapor Deposition. *J. Am. Chem. Soc.* **2011**, *133*, 5232–5235.
42. Tian, Y.; Nasibulin, A. G.; Aitchison, B.; Nikitin, T.; Pfaler, J.; Jiang, H.; Zhu, Z.; Khriachtchev, L.; Brown, D. P.; Kauppinen, E. I. Controlled Synthesis of Single-Walled Carbon Nanotubes in an Aerosol Reactor. *J. Phys. Chem. C* **2011**, *115*, 7309–7318.
43. Zhu, Z.; Jiang, H.; Susi, T.; Nasibulin, A. G.; Kauppinen, E. I. The Use of $NH_3$ To Promote the Production of Large-Diameter Single-Walled Carbon Nanotubes with a Narrow (*n,m*) Distribution. *J. Am. Chem. Soc.* **2011**, *133*, 1224–1227.
44. Oyama, Y.; Saito, R.; Sato, K.; Jiang, J.; Samsonidze, G. G. Gruneis, A.; Miyauchi, Y.; Maruyama, S.; Jorio, A.; Dresselhaus, G.; *et al.* Photoluminescence Intensity of Single-Wall Carbon Nanotubes. *Carbon* **2006**, *44*, 873–879.
45. Brik, Y.; Kacimi, M.; Ziyad, M.; Bozon-Verduraz, F. Titania-Supported Cobalt and Cobalt−Phosphorus Catalysts: Characterization and Performances in Ethane Oxidative Dehydrogenation. *J. Catal.* **2001**, *202*, 118–128.
46. Cheung, C. L.; Kurtz, A.; Park, H.; Lieber, C. M. Diameter-Controlled Synthesis of Carbon Nanotubes. *J. Phys. Chem. B* **2002**, *106*, 2429–2433.
47. Jeong, G. H.; Suzuki, S.; Kobayashi, Y.; Yamazaki, A.; Yoshimura, H.; Homma, Y. Size Control of Catalytic Nanoparticles by Thermal Treatment and Its Application to Diameter Control of Single-Walled Carbon Nanotubes. *Appl. Phys. Lett.* **2007**, *90*, 043108.
48. Zhu, W. M.; Borjesson, A.; Bolton, K. DFT and Tight Binding Monte Carlo Calculations Related to Single-Walled Carbon Nanotube Nucleation and Growth. *Carbon* **2010**, *48*, 470–478.
49. Nasibulin, A. G.; Pikhitsa, P. V.; Jiang, H.; Kauppinen, E. I. Correlation between Catalyst Particle and Single-Walled Carbon Nanotube Diameters. *Carbon* **2005**, *43*, 2251–2257.
50. Rehr, J. J.; Kas, J. J.; Vila, F. D.; Prange, M. P.; Jorissen, K. Parameter-Free Calculations of X-ray Spectra with FEFF9. *Phys. Chem. Chem. Phys.* **2010**, *12*, 5503–5513.
51. Frenkel, A. I.; Hills, C. W.; Nuzzo, R. G. A View from the Inside: Complexity in the Atomic Scale Ordering of Supported Metal Nanoparticles. *J. Phys. Chem. B* **2001**, *105*, 12689–12703.
52. Xiang, Y.; Sun, D. Y.; Gong, X. G. Generalized Simulated Annealing Studies on Structures and Properties of $Ni_n$ ($n = 2-55$) Clusters. *J. Phys. Chem. A* **2000**, *104*, 2746–2751.
53. Knickelbein, M. B. Electric Dipole Polarizabilities of $Ni_{12-58}$. *J. Chem. Phys.* **2001**, *115*, 5957–5964.
54. Apra, E.; Fortunelli, A. Density-Functional Calculations on Platinum Nanoclusters: $Pt_{13}$, $Pt_{38}$, and $Pt_{55}$. *J. Phys. Chem. A* **2003**, *107*, 2934–2942.
55. Singh, R.; Kroll, P. Structural, Electronic, and Magnetic Properties of 13-, 55-, and 147-Atom Clusters of Fe, Co, and Ni: A Spin-Polarized Density Functional Study. *Phys. Rev. B: Condens. Matter Mater. Phys.* **2008**, *78*, 245404.
56. Wang, Q.; Lim, K. H.; Yang, S. W.; Yang, Y. H.; Chen, Y. Atomic Carbon Adsorption on Ni Nanoclusters: A DFT Study. *Theor. Chem. Acc.* **2011**, *128*, 17–24.
57. Helveg, S.; Lopez-Cartes, C.; Sehested, J.; Hansen, P. L.; Clausen, B. S.; Rostrup-Nielsen, J. R.; Abild-Pedersen, F.;

Norskov, J. K. Atomic-Scale Imaging of Carbon Nanofibre Growth. *Nature* **2004**, *427*, 426–429.
58. Sharma, R.; Iqbal, Z. *In Situ* Observations of Carbon Nanotube Formation Using Environmental Transmission Electron Microscopy. *Appl. Phys. Lett.* **2004**, *84*, 990–992.
59. Hofmann, S.; Sharma, R.; Ducati, C.; Du, G.; Mattevi, C.; Cepek, C.; Cantoro, M.; Pisana, S.; Parvez, A.; Cervantes-Sodi, F.; *et al. In Situ* Observations of Catalyst Dynamics during Surface-Bound Carbon Nanotube Nucleation. *Nano Lett.* **2007**, *7*, 602–608.
60. Lim, S.; Ciuparu, D.; Chen, Y.; Pfefferle, L.; Haller, G. L. Effect of Co-MCM-41 Conversion to Cobalt Silicate for Catalytic Growth of Single Wall Carbon Nanotubes. *J. Phys. Chem. B* **2004**, *108*, 20095–20101.
61. Lim, S.; Ciuparu, D.; Chen, Y.; Yang, Y. H.; Pfefferle, L.; Haller, G. L. Pore Curvature Effect on the Stability of Co-MCM-41 and the Formation of Size-Controllable Subnanometer Co Clusters. *J. Phys. Chem. B* **2005**, *109*, 2285–2294.
62. Lim, S.; Yang, Y. H.; Ciuparu, D.; Wang, C.; Chen, Y.; Pfefferle, L.; Haller, G. L. The Effect of Synthesis Solution pH on the Physicochemical Properties of Co Substituted MCM-41. *Top. Catal.* **2005**, *34*, 31–40.
63. Ci, L.; Wei, J.; Wei, B.; Liang, J.; Xu, C.; Wu, D. Carbon Nanofibers and Single-Walled Carbon Nanotubes Prepared by the Floating Catalyst Method. *Carbon* **2001**, *39*, 329–335.
64. Ren, W.; Li, F.; Bai, S.; Cheng, H. M. The Effect of Sulfur on the Structure of Carbon Nanotubes Produced by a Floating Catalyst Method. *J. Nanosci. Nanotechnol.* **2006**, *6*, 1339–1345.
65. Wei, J.; Zhu, H.; Jia, Y.; Shu, Q.; Li, C.; Wang, K.; Wei, B.; Zhu, Y.; Wang, Z.; Luo, J. The Effect of Sulfur on the Number of Layers in a Carbon Nanotube. *Carbon* **2007**, *45*, 2152–2158.
66. Sundaram, R. M.; Koziol, K. K. K.; Windle, A. H. Continuous Direct Spinning of Fibers of Single-Walled Carbon Nanotubes with Metallic Chirality. *Adv. Mater.* **2011**, *23*, 5064–5068.
67. Perdew, J. P.; Burke, K.; Ernzerhof, M. Generalized Gradient Approximation Made Simple. *Phys. Rev. Lett.* **1996**, *77*, 3865–3868.
68. Kresse, G.; Furthmuller, J. Efficiency of *Ab-Initio* Total Energy Calculations for Metals and Semiconductors Using a Plane-Wave Basis Set. *Comput. Mater. Sci.* **1996**, *6*, 15–50.
69. Kresse, G.; Furthmuller, J. Efficient Iterative Schemes for *Ab Initio* Total-Energy Calculations Using a Plane-Wave Basis Set. *Phys. Rev. B: Condens. Matter Mater. Phys.* **1996**, *54*, 11169–11186.
70. Blöhl, P. E. Projector Augmented-Wave Method. *Phys. Rev. B: Condens. Matter Mater. Phys.* **1994**, *50*, 17953–17979.
71. Kresse, G.; Joubert, D. From Ultrasoft Pseudopotentials to the Projector Augmented-Wave Method. *Phys. Rev. B: Condens. Matter Mater. Phys.* **1999**, *59*, 1758–1775.